Received November 12, 2018, accepted December 12, 2018, date of publication December 18, 2018,
date of current version January 7, 2019.

Digital Object Identifier 10.1109/ACCESS.2018.2887113

Comparative Study of Inkjet-Printed Silver Conductive Traces With Thermal and Electrical Sintering

PABLO ESCOBEDO[1], **MIGUEL A. CARVAJAL**[1], **JESÚS BANQUERI**[1], **ANTONIO MARTÍNEZ-OLMOS**[1], **LUIS FERMÍN CAPITÁN-VALLVEY**[2], **AND ALBERTO J. PALMA**[1]

[1]Department of Electronics and Computer Technology, University of Granada, 18071 Granada, Spain
[2]Department of Analytical Chemistry, University of Granada, 18071 Granada, Spain

Corresponding author: Alberto J. Palma (ajpalma@ugr.es)

This work was supported in part by the Spanish Ministry of Economics and Competitiveness under Grant CTQ2016-78754-C2-1-R. The work of P. Escobedo was supported by the Spanish Ministry of Education, Culture, and Sport for a Predoctoral grant under Grant FPU13/05032.

ABSTRACT Thermal sintering has traditionally been the most popular sintering method to enhance conductivity after the printing process in the manufacturing of printed electronics. Nevertheless, in recent years, there has been a growing interest in electrical sintering as an alternative method to overcome some of the limitations of thermal curing. This paper makes a comparative study of both sintering methods in terms of surface morphology, electrical dc conductance, and radiofrequency performance for different applied voltage waveforms. To this end, microstrip transmission lines have been inkjet-printed using nanoparticle-based silver ink on flexible polyimide substrate. The traces have been tested under different sintering conditions, achieving electrical sintering resistivity values only 2.3 times higher than that of bulk silver. This implies a 62% reduction in comparison with the best resistivity value achieved using thermal sintering in our samples. The main novelty of this contribution lies in the analysis of RF behavior as a function of electrical sintering conditions. Lower resistivities have been achieved with slower voltage ramps or allowing higher density current during sintering. It has also been proved that electrically sintered lines have similar RF performance than high-temperature thermally sintered lines in terms of insertion losses, regardless of their very different surface topology. Therefore, we can take advantage of the benefits that electrical sintering offers over thermal sintering regarding significant shorter sintering times maintaining suitable RF performance.

INDEX TERMS Electrical sintering, inkjet printing, microstrip transmission line, silver nanoparticle ink, thermal sintering.

I. INTRODUCTION

Printed Electronics (PE) offer a cost-effective, high-throughput and waste-free attractive alternative to conventional electronic device manufacturing techniques such as lithography or etching. In fact, the PE market was valued at \$3.13 Billion in 2015 and is expected to reach \$12.10 Billion by 2022, at an estimated compound annual growth rate (CAGR) of 22.38% from 2016 to 2022 [1]. The major benefit of PE is that the overall process only consists of two stages, i.e. printing and sintering, allowing a reduction of time and cost [2]. PE has a place in various application fields, among which we can highlight the manufacturing of printed photovoltaics and OLEDs [3]–[5], RFID tags [6]–[9], printed sensors [10]–[12], electronics and components such as memories [13], antennas [14], [15], batteries [16], diodes [17], transistors [18], wiring and interconnects [19] or passive components [20], [21].

Among the different printing techniques for the manufacturing of PE, inkjet printing technology has raised great attention in recent years since it allows accurate deposition of micro and nanomaterials into functional arrangement in a maskless, additive patterning and non-contact approach [22], [23]. Among all the potential candidates of printable conductive materials, silver-based metal nanoparticle (NP) inks are the most widely used due to its high electrical conductivity and low oxidation rate [24], [25]. The use of

2169-3536 © 2018 IEEE. Translations and content mining are permitted for academic research only.
Personal use is also permitted, but republication/redistribution requires IEEE permission.
See http://www.ieee.org/publications_standards/publications/rights/index.html for more information.

metallic inks for PE implies the need for a post-printing treatment (i.e. sintering) in order to promote NP coalescence and adhesion by removing non-conductive organic components to enhance conductivity [26]. The easiest and most common method for metallic NP-based ink curing is thermal sintering [27], which consists of exposing printed patterns to heat, either on a hot plate or inside an oven. Nevertheless, thermal sintering is a time-consuming process with other disadvantages, e.g. some substrates can suffer from shrinkage when exposed to typical sintering temperatures, and there can be undesired gas emission from the substrate during the process. Moreover, it is not an area-specific process, that is, the whole structure needs to be sintered [28]. To overcome some of these limitations, many other alternative sintering approaches have been proposed [29], [30] such as laser and photonic sintering [31], microwave and plasma sintering [32], chemical sintering [33] or electrical sintering [28], [34]. This latter sintering method has some key advantages that can be summarized in short sintering times and reduced substrate heating, since heat generates only within the nanoparticle layer [35].

In the literature there are numerous studies on thermal and electrical sintering effects of silver NP-based printed structures in terms of electrical resistance [36]–[38] or morphology [39]–[41]. Concerning the characterization of printing techniques for RF and microwave applications, there are some reports on cooper and silver-based inkjet-printed structures such as planar transmission lines [42]–[48], split-ring resonators [49] and other passive RF structures [50], as well as printed antennas for RFID applications [8], [51]–[56]. Nevertheless, not much is known about the effects of the sintering process on printed structures for RF and microwave applications. In this study, flexible printed microstrip lines were manufactured by inkjet printing on polyimide (PI) substrates using a silver-based NP ink. Printed lines were sintered both thermally and electrically, and various characteristics of sintered lines including surface morphology and electrical DC conductance were studied. Moreover, the RF performance of the printed lines was analyzed to estimate its potential applicability in RF applications such as radio frequency identification (RFID) and wireless body area networks (WBANs).

II. EXPERIMENTAL DETAILS

A. MICROSTRIP LINES DESIGN AND FABRICATION

To test and characterize sintered printed patterns, microstrip lines were designed and fabricated by inkjet printing using a Dimatix Materials Printer DMP-2831TM (Fujifilm Dimatix Inc, Santa Clara, USA). The microstrip lines were printed on polyimide Kapton® HN substrate (DuPont™, Wilmington, DE, USA). We employed a 75 μm-thick Kapton film with one side metallized with 30 nm aluminum to act as the ground plane (IM301835, GoodFellow, Huntingdon, England). The patterns were inkjet-printed using SunTronic U5603 silver ink (Sun Chemical, New Jersey, USA). With a particle size of 80 nm and viscosity around 10-13 cPs at 25°C, this nanoparticle-based silver ink has a 20% solid Ag content ethanol and ethanediol. According to the manufacturer, after curing at 150–300 °C the ink can achieve resistivities between 5-30 $\mu\Omega \cdot$ cm. As for printing parameters, a drop-to-drop (DTD) space of 25 μm was used, drop diameter on landing was approximately 50 μm, and substrate temperature was set to 40 °C while printing. The printhead had 21 μm diameter nozzles with drop sizes of 10 pL.

An additional microstrip line was designed and fabricated as a reference strip on double sided PCB with FR4 substrate. A mechanical milling machine model ProtoMat® S100 (LPKF Laser & Electronics AG, Garbsen, Germany) was employed for this purpose. The FR4 substrate had a relative permittivity of $\varepsilon_r = 4.6$ and a loss tangent of ta $\delta = 0.015$. Metallization layer was 35 μm thick copper with a conductivity of $\sigma = 4.6 \times 10^7$ S/m.

Microstrip lines are a type of transmission lines used for Electromagnetic (EM) wave propagation and here used as a test structure at radiofrequency. Fig. 1a shows the typical geometry of this structure, which consists of three layers: a dielectric substrate with a continuous ground plane on one side and a metallic signal conductor on the other side. The characteristic impedance of the microstrip line depends on the conducting strip width, height and length, as well as on the substrate properties such as thickness, relative permittivity and dissipation factor [57]. Line Calculator tool from Advanced Design System (ADS) simulator (Agilent Technologies, Santa Clara, CA, USA) was used for the combination of the employed substrate and ink to find the geometric dimensions leading to the desired 50 Ω characteristic impedance. Conductivity value was set to the corresponding minimum resistivity value achievable with the ink according to the manufacturer, that is, 5 $\mu\Omega \cdot$ cm. Table 1 shows the geometric dimensions obtained with ADS software for the rigid FR4 and the flexible inkjet-printed microstrip lines. According to the inkjet-printed model previously reported in our research group [6], the irregularity in the contribution of the outer part of the lines to the total width has to be taken into account if the printed element is comparable in size with the diameter of one printed drop. In this case, the drop-to-drop distance was DTD = 25 μm and the targeted width was 169 μm, where the outer drop contribution was taken into account as depicted in Fig. 1b.

TABLE 1. Microstrip lines dimensions.

Materials	Substrate		Conducting strip	
	Thickness	ε_r	Length l	Width w
Copper on FR4 substrate	1.5 mm	4.6	46.5 mm	2.70 mm
Silver ink on PI substrate	75 µm	3.5	52.1 mm	168.9 µm

Microstrip lines dimensions computed with Line Calculator from ADS to obtain a characteristic impedance of 50 Ω for the two different material combinations used.

A two-step printing process was carried out for the fabrication of the microstrip lines. Firstly, the squared pads were

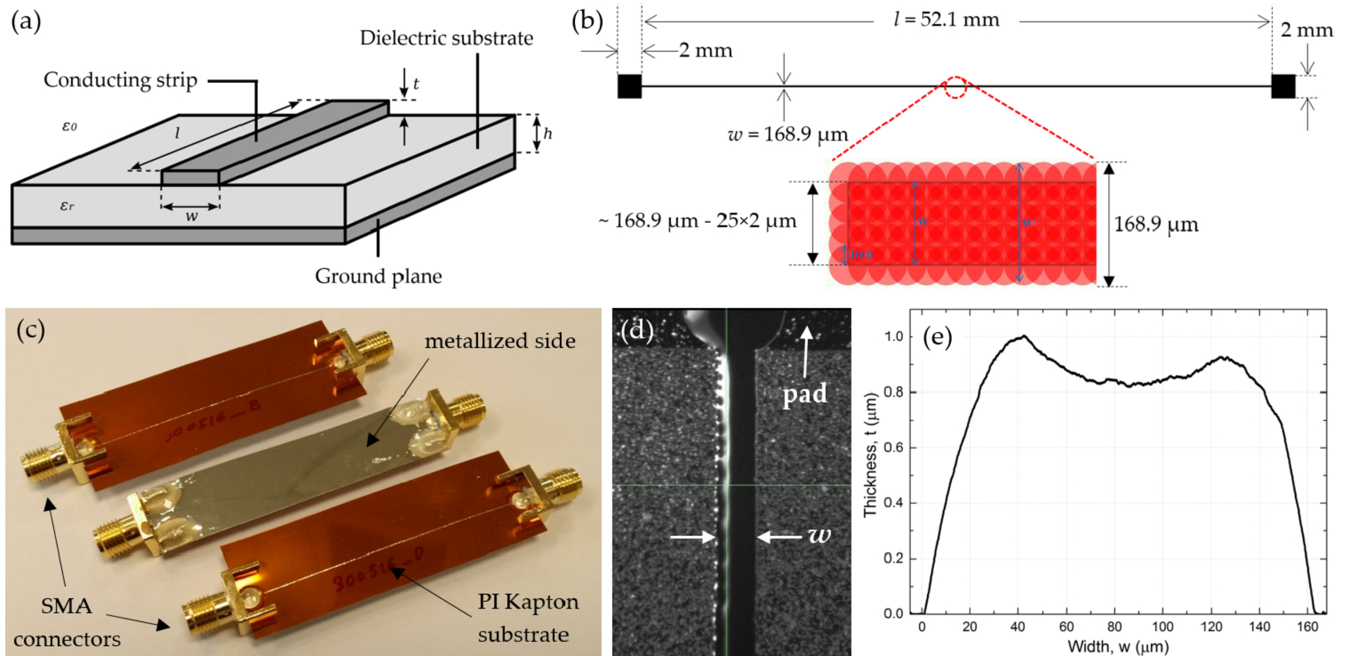

FIGURE 1. (a) Geometry of a microstrip line composed of three layers: conducting strip with length l, width w and thickness t; dielectric layer with thickness h and relative permittivity ε_r; and ground plane. (b) Footprint of the designed microstrip line with dimensions. (c) Image of some inkjet-printed microstrip lines on PI metallized film with attached SMA connectors. (d) Picture with the Dimatix fiducial camera of a printed microstrip line before sintering. (e) Example of a measured printed microstrip line profile.

printed and cured at 160 °C during 60 minutes in a convection air oven Venticell VC55 (MMM Medcenter Einrichtungen GmbH, Munich, Germany), in accordance with our previous research in this field [6]. Then, the lines between the pads were printed. Subminiature Version A (SMA) edge connectors were attached using silver Epoxy EPO-TEK® H20E (Epoxy Technology Inc., Billerica, USA) on both ends of the printed lines in order to characterize their frequency response using a Network Analyzer (ENA) as shown in Fig. 1c.

For structural characterization, the surface roughness of the printed Ag lines was measured by profiling areas of 700×500 μm^2 with a non-contact 3D surface profiler confocal PLu Sensofar (Sensofar Tech., Barcelona, Spain). Fig. 1e shows an example of a randomly measured profile of a printed microstrip. We obtained a measured average width of 169 ± 3 μm, very close to the designed value. The measured average thickness was 0.9 ± 0.1 μm, in line with previous works using the same combination of substrate and ink [6].

B. THERMAL SINTERING

Six sintering temperatures were considered, from 100 °C to 200 °C in steps of 20 °C. Furthermore, two different situations were studied: (i) sintering with temperature ramp up to the final temperature and (ii) sintering with temperature step, that is, the printed samples are introduced in the oven once it has reached the desired final temperature. In both cases, the final temperature was kept during 60 minutes and then the oven was automatically turned off. The samples were kept inside the oven until temperature was gradually reduced to approximate ambient temperature.

The sintering process was monitored inside the oven by connecting a 34970A data acquisition unit (Agilent Technologies, Santa Rosa, California, USA) to the sintered pads of the printed lines through clamps and heat resistant cables. The acquisition unit was configured to scan and log four channels during the curing process. Three of them were dedicated to three printed patterns, while the fourth one was connected to a Pt1000 resistance temperature detector (RTD). The minimum interval scanning time achieved with the equipment was 1.4 seconds. Resistivity of the printed lines was calculated based on dimensional measurements and the measured resistance [58]. The equation to calculate resistivity ρ is:

$$\rho = R\frac{A}{l}, \tag{1}$$

where R is the measured resistance of the printed trace, A is the cross-sectional area of the printed trace and l refers to its length. Cross-sectional area of the printed traces was calculated by measuring the lines thickness and width. Three profile measurements were taken for one microstrip line per temperature, making a total of 18 measurements. The cross-sectional area used for the resistivity calculations was the average of all the measurements.

C. ELECTRICAL SINTERING

The resistance of the printed lines just after printing was too high to be electrically sintered, therefore a thermal

pre-sintering phase was applied to establish an initial level of conductance prior to the application of electrical current. Consequently, the lines were preheated in the oven at 100 °C from 3 to 5 minutes. This preheating time determined the initial resistance of the printed line, which ranged from hundreds of ohms to several kΩ. After this, electrical sintering was carried out. A DC Power Analyzer (N6705A, Keysight Tech., Santa Clara, CA, USA) was employed to apply voltage to the printed lines for electrical sintering. By applying a potential difference to both ends of the line, the generated electrical power accelerates the free electrons to move through the conductive ink track. The collisional energy of free electros with silver nanoparticles in the conductive ink is then changed to thermal energy by Joule heating [34].

Two different voltage waveforms (pulse and ramp) were tested in order to cure the patterns using different voltage and current values. The DC power analyzer was employed in data logger mode so that voltage and current values were recorded during the electrical sintering process. The maximum allowed current influences the final resistivity of the line and protects it from burning out by abrupt decrease of resistance [59]. This parameter was controlled using a built-in function in the DC power analyzer, the so-called over-current protection (OCP) feature. With OCP enabled, the DC power analyzer disabled the output if the output current reached the current limit setting. Several OCP from 0.35 A to 0.6 A were configured during electrical sintering for the different voltage waveforms. It was experimentally found that when OCP was greater than 0.6 A, the line patterns were always burned and blown out. In our samples, maximum current densities from 2280 A/mm^2 to 3920 A/mm^2 were obtained for 0.35 to 0.6 A of OCP. Another parameter that was controlled during the tests was the slope of the applied voltage waveform, from 12000 V/s (corresponding to the voltage pulse) down to 1 V/s using the ramp waveform up to 20 V. A maximum voltage of 20 V was experimentally selected after verifying that sintering was achieved before reaching this voltage in our preliminary tests with slow voltage ramps in thermal pre-sintered patterns.

D. RF CHARACTERIZATION

A RF network analyzer ENA model E5071C (Keysight Tech., Santa Clara, CA, USA) was used to measure the RF response of the printed microstrip lines. The analyzer was employed along with a custom-made wood structure to fix the probes and avoid mechanical stress of the lines. The N4431B RF electronic calibration module (ECal) was employed along with the Network Analyzer for calibration purposes. RF performance was assessed by measuring the forward transmission coefficient S_{21}, which is a measure of the signal coming out port 2 relative to the RF stimulus entering port 1 [57]. In other words, S_{21} is the ratio of the transmitted voltage to the incident voltage when the output is terminated in a perfect Z_0 (a load that equals the characteristic impedance of the DUT, which is in our case the microstrip line). S_{21} means transmission loss or gain and will be negative if DUT has a loss, and positive if DUT has a gain.

ADS software based on momentum method was used to simulate the RF performance of the printed lines to assess the validity of the measurements, including their metallization geometry, surface roughness, conductivity and the influence of the substrate.

III. RESULTS AND DISCUSSION

A. LINE SURFACE CHARACTERIZATION

The surface morphology of printed structures is deeply related to the process conditions: both printing and sintering. Fig. 2a presents the average surface roughness of the printed lines for various sintering methods along with 2D surface morphology images of each case. This surface study can provide an extended information of the line morphology after sintering. No significant differences were observed between ramp and step in thermal sintering at any studied sintering temperature nor between ramp and pulse in electrical sintering with the same OCP. The surface roughness increased significantly from 200 ± 40 nm for thermal sintering to 320 ± 50 nm for electrical sintering with OCP = 0.4 A, stepping up to an average of 690 ± 80 nm with OCP = 0.6 A. Fig. 2b-d show the 3D surface morphology images extracted from the non-contact surface profiling system. It can be seen in Fig. 2b the relatively flat morphology derived from the thermal curing process, while Fig. 2c and 2d show more complex morphologies as a result of current flows during electrical sintering. In the case of OCP = 0.6 A, Fig. 2d reveals micro-scale cluster islands formed with silver in the wake of abrupt temperature changes within the printed structure due to the application of large current flows during electrical sintering.

B. ELECTRICAL DC CHARACTERIZATION

Resistivity change of the printed lines during thermal sintering with temperature ramp is depicted in Fig. 3a, while Fig. 3b shows the same experiment but using temperature step as described in the experimental section. In both cases, a set of three printed lines were sintered at each temperature. As expected, the higher temperature, the faster changes in resistivity. We can divide each graph of thermal sintering process into three phases: (i) the first in which the patterns are still non-conductive and the instrument measures an infinite resistance; (ii) the second is a transition phase, where resistivity quickly decreases in a short period of time and the actual sintering phenomenon occurs; (iii) finally, a third region with low resistivity changes. These regions can be associated to the two basic stages of any sintering process [36]. The first region corresponds to the first sintering stage, which consists of the thermal decomposition and removing of surfactants. In this stage the nanoparticles are still separated by the outer organic layers, so they do not touch each other and therefore the resistance is too high. In the second stage, which corresponds to the other two regions in our graph, the nanoparticle protective shells are removed and the diffusion and recrystallization

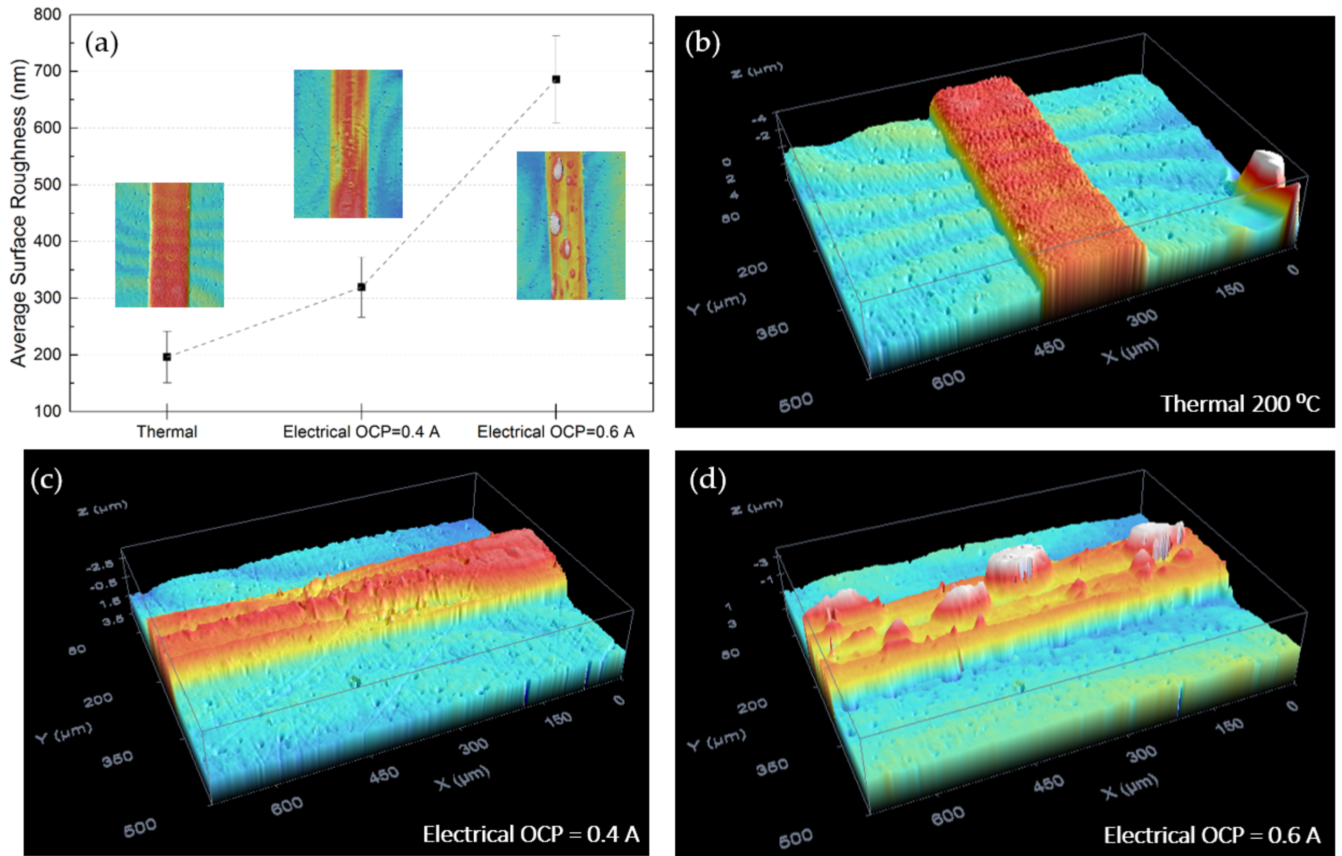

FIGURE 2. (a) Average surface roughness and profiled surface morphology images of (b) thermally sintered lines at 200°C, (c) electrically sintered lines with OCP = 0.4 A and (d) electrically sintered lines with OCP = 0.6 A.

processes are dominant. At the start of this phase, many new electrical paths between the nanoparticles are created within a short period of time, so the resistivity quickly decreases. After this, the sintering process slows down and the resistivity reduces much more slowly.

Further analysis was done to study the starting times of the thermal sintering process corresponding to the above mentioned first sintering phase. Starting time was considered as the moment when the data acquisition unit began measuring a resistance value below 1 GΩ. The obtained values for the different temperatures ranged from 90 s (200 °C) to 500 s (100 °C) for temperature step, obtaining longer interval for temperature ramps. The first remarkable fact was that sintering phenomenon started long before in the case of temperature step, which is expected since the oven already had a high temperature when the samples were placed inside it. In this case, the patterns started sintering just after 88 seconds for the highest temperature, while they needed more than 8 minutes for the lowest temperature. In other words, with temperature step the time required to start the sintering process was closely correlated with the temperature. On the other hand, with temperature ramp almost all printed structures started the sintering process at approximately the same time, around 15 minutes after the samples are introduced into the oven. This was true for all temperatures except for the lowest one, 100 °C. At this temperature value, the starting time was about three minutes higher than the average starting time of the other cases. This suggests that the reached value of temperature was not high enough to cause the beginning of the sintering process, as it happened with higher temperature values. As a consequence, the printed silver tracks needed more time to remove the protective surfactants layer. Regarding the time intervals corresponding to the second phase for temperature step, where the actual sintering phenomenon occurs, curing times ranged from 120 s to 180 s (for T > 120 °C) in the fastest case up to 15 minutes (T = 100 °C). These periods were estimated from the moment when the data acquisition unit began measuring a resistance value below 1 GΩ until the moment when the achieved resistivity was twice the value of the final resistivity in each case. In the case of temperature ramp, we have not compared these intervals because of the ramp duration itself, which is dependent of the target temperature, depending on the thermal sintering conditions. Fig. 4 depicts the average measured resistivity of each set of microstrip lines for the six final temperatures and the two cases considered: ramp and step of temperature. As it can be observed, best resistivity values were achieved for the temperature step. The difference is

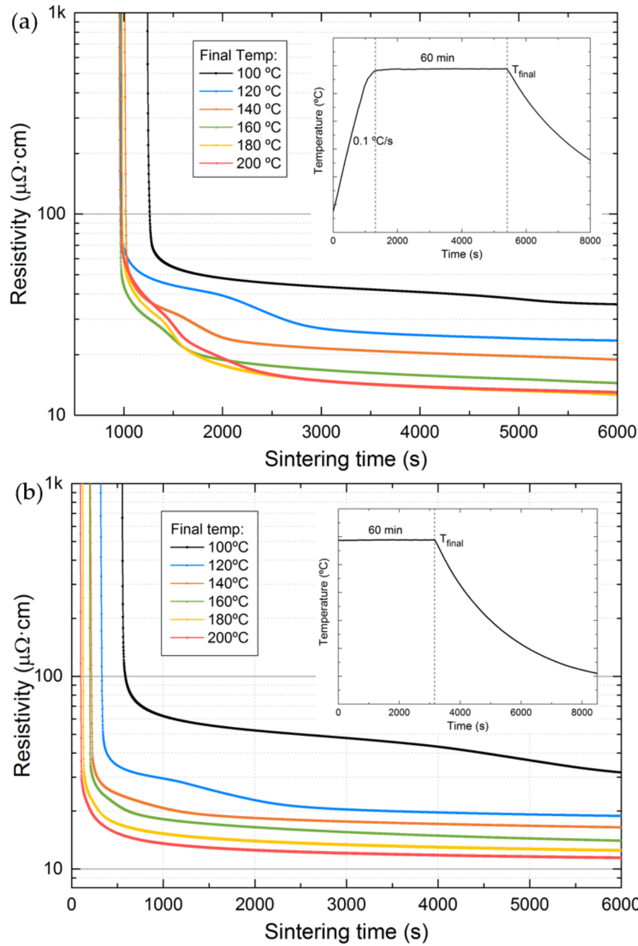

FIGURE 3. Resistivity change of the printed lines during thermal sintering with (a) temperature ramp and (b) temperature step.

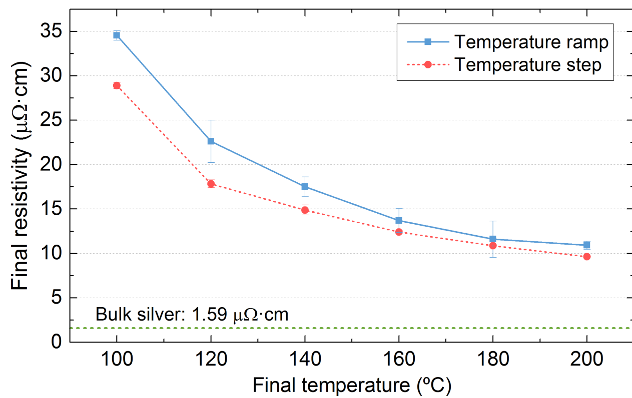

FIGURE 4. Final resistivities as a function of final sintering temperatures in the cases of temperature ramp and temperature step during the thermal sintering process.

more significant for lower final temperatures than for higher ones. In the case of temperature ramp, the best resistivity value achieved was $\rho = 10.9 \pm 0.4\ \mu\Omega \cdot \text{cm}$ for 200 °C, which is roughly seven times the value of bulk silver resistivity, $1.59\ \mu\Omega \cdot \text{cm}$ [60]. The lowest value of $\rho = 9.41 \pm 0.12\ \mu\Omega \cdot \text{cm}$ was achieved with temperature step at 200 °C, which is about six times the value of bulk silver. These results

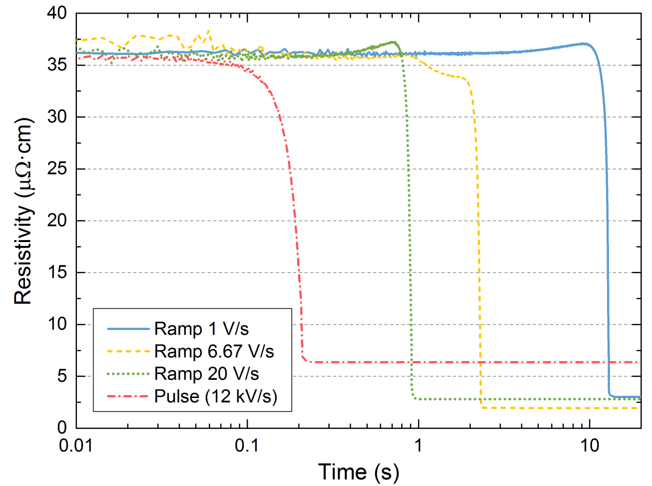

FIGURE 5. Some examples of resistivity change of the printed lines during electrical sintering for different voltage ramps up to 20 V. Pulse voltage will be considered as a ramp with a slope of 12 kV/s.

are consistent with the resistivity of 5-30 $\mu\Omega \cdot \text{cm}$ specified in the SunTronic ink manufacturer datasheet. Also, the results are in the same order as those reported in previous studies [27], [40], [61], [62]. Measured resistivities are higher than bulk silver resistivity because printed silver has smaller grain size and higher porosity than bulk silver. In consequence, electrons scatter more at the grain boundaries of printed silver than on bulk silver [6], [63]. For electrical sintering, Fig. 5 shows the resistivity transients for voltage ramps with different slopes. Electrical sintering times were extracted from these transients and also analyzed as a figure of merit to be compared with thermal sintering. Similar as in the case of thermal sintering, curing intervals were estimated from the moment when the voltage waveform was applied until the moment when the achieved resistivity was twice the value of the final resistivity. Table 2 collects the averaged sintering times for different ramp slopes, showing a reduction of time when slope increases. These results are in good agreement with previously reported studies [34], [59], [64] and reveal one of the great advantages of electrical sintering over thermal curing.

TABLE 2. Electrical sintering times.

Waveform type	Slope (V/s)	Average sintering time (s)
Voltage ramp	1	12.2 ± 1.8
	6.67	2.05 ± 0.07
	20	0.82 ± 0.07
Voltage pulse	12k	0.22 ± 0.03

Average sintering times for different voltage ramps up to 20 V. Uncertainty was calculated as data standard deviation.

Fig. 6 reports the final resistivity results of electrical sintering applied to the inkjet printed silver structures (50 samples). On the one hand, Fig. 6a shows the measured final resistivities

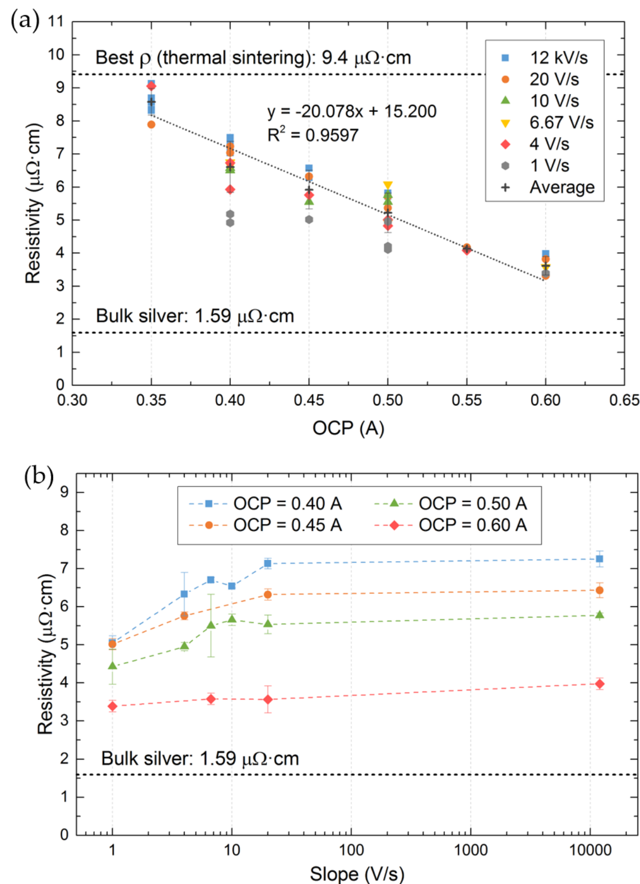

FIGURE 6. **(a) Final resistivities as a function of configured OCP limits for different cases of waveform slopes during electrical sintering. (b) Final resistivities as a function of waveform slopes during electrical sintering for various cases of OCP limits.**

of the lines as a function of the configured OCP for various voltage waveform slopes ranging from 12000 V/s (maximum voltage slope obtained in pulse mode) down to 1 V/s. On the other hand, final resistivities as a function of the waveform slopes are shown in Fig. 6b for different OCP values. From the graph in Fig. 6a we can note that final resistivity is reduced with increasing current limit. This is justified by the fact that higher current densities are associated with higher temperatures within the printed structure [65], leading to a more progressed sintering and lower resistivities as previously obtained during thermal sintering. At the highest OCP limit of 0.6 A, an average resistivity of 3.6 ± 0.3 $\mu\Omega \cdot$ cm was achieved, which is about 2.3 times larger than the bulk Ag resistivity. In any case, resistivity values obtained during electrical sintering are always lower than the best case obtained using thermal sintering, which was around 9.4 $\mu\Omega \cdot$ cm with 200 °C temperature step. In comparison with this value, we have achieved a substantial resistivity reduction of 62% using electrical sintering. According to the linear fitting applied to the experimental data, the predicted current limit to obtain the same resistivity as the best case of thermal sintering would be 0.28 A.

Regarding the dependence of final resistivity upon voltage ramp slope (Fig. 6b), our findings point out that best resistivity values are achieved using lower slopes during electrical sintering. This can be attributed to the fact that sintering characteristics are also influenced by the mechanical strength of printed structures, as previously reported in the literature [39], [59]. In this context, sintering performance is improved using lower waveform slopes, suggesting that electrical sintering of the printed lines at a slower pace results in an increase of its mechanical strength as compared to the abrupt change produced when using voltage pulses. Moreover, we can observe that this difference between resistivities at different slopes is reduced with increasing OCP, shown as a lower slope for increasing OCP in Fig. 6b. It seems that at OCP = 0.6 A, the delivered power is so high that the final resistivity is nearly independent from the voltage ramp slope.

C. RF PERFORMANCE

Fig. 7 reports, for frequencies between 100 kHz and 6 GHz, the attenuation and insertion loss per unit length extracted from measurements with the RF network analyzer for printed microstrips featuring different sintering methods. Three particular frequencies (868 MHz, 2.4 GHz and 5 GHz) have been selected for a more detailed analysis as the most representative ones in the field of RFID and WBANs applications. To provide theoretical support to our experimental results, numerical simulations were carried out using the physical dimensions, surface roughness and experimental DC conductivities of the microstrips. Fig. 8 shows very good agreement between them, both for thermal and electrical sintering.

It is apparent from Fig. 7a the decay of the transmission parameter S_{21} as frequency increases, which is related to the loss phenomena. In a transmission line there are three types of losses: the dielectric substrate losses, the conductor (or ohmic) losses and the radiation losses [57]. For typical substrates thicknesses used in PE, ohmic losses become more significant as the frequency rises and they usually dominate over dielectric and radiation losses [66]. For this reason, the decay in S_{21} can be attributed to losses in the conductor, which are a result of several factors such as conductivity, surface roughness and skin effect. This behavior is fulfilled for all the lines at the measured frequency range.

As for the FR4 microstrip line, we can observe that its losses are significantly lower than inkjetted ones. In the first place, there is a clear difference in the substrate thickness, which is 1.5 mm for the FR4 lines and about 75 μm for the inkjet-printed lines. On the other hand, conducting strip conductivity and thickness are larger for the rigid FR4 lines (copper has a resistivity of 1.68 $\mu\Omega \cdot$ cm) than for the printed lines. These results confirm that ohmic losses related to conducting layer properties play a critical role on RF performance.

Fig. 7b details the averaged insertion losses for the different sintering methods at the three selected frequencies of interest, which are collected in Table 3. It can be observed that the greatest losses were obtained for the microstrip lines thermally sintered at 100 °C, which was the lowest

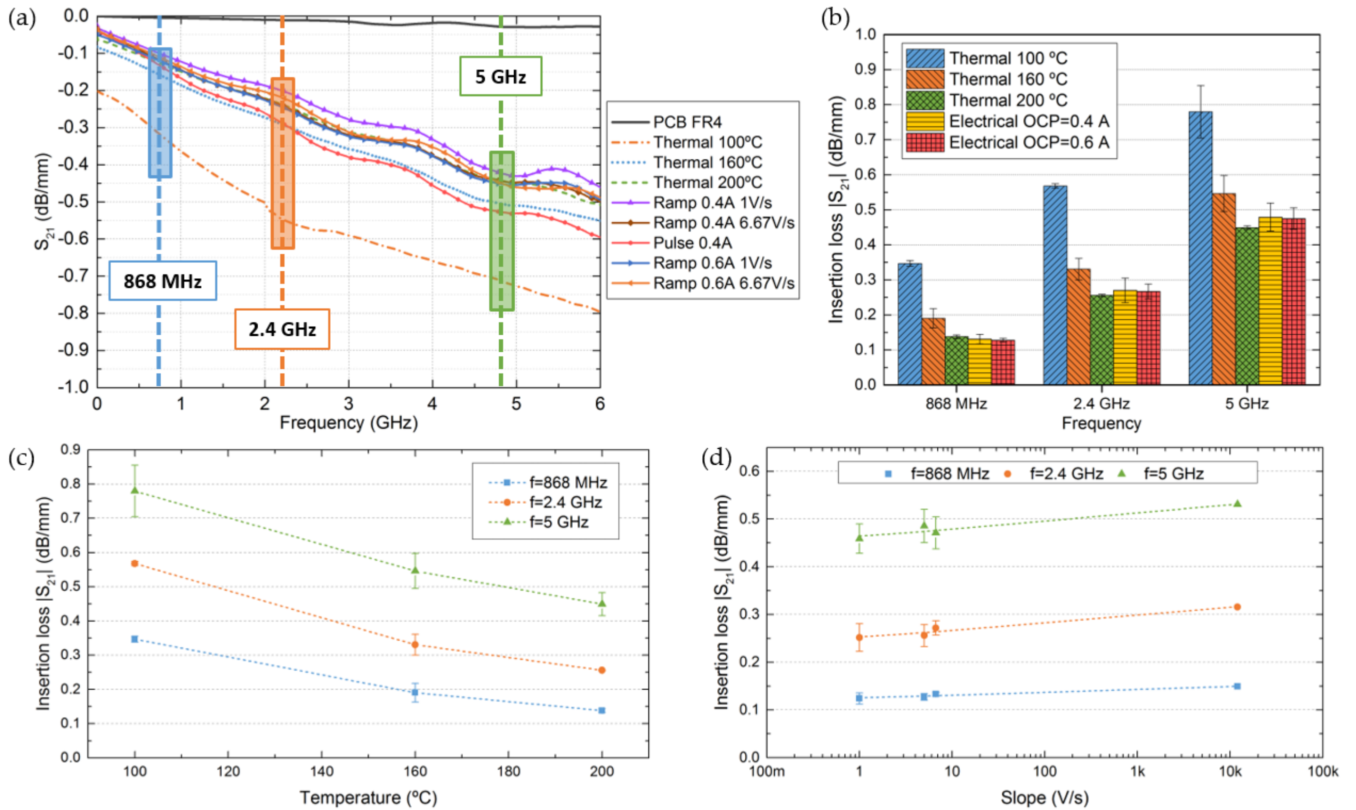

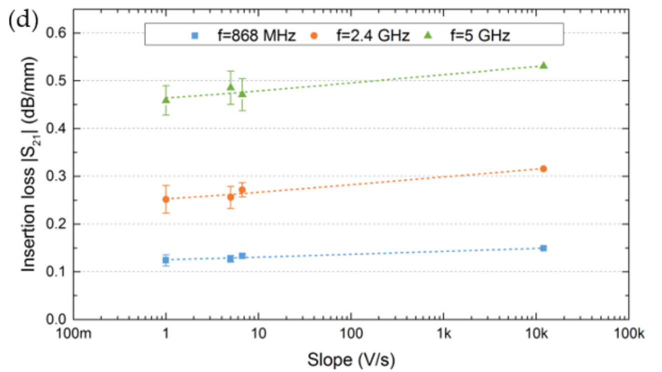

FIGURE 7. (a) Attenuation of various microstrip lines sintered both thermally and electrically under different conditions. The vertical lines refer to the three frequencies that will be analyzed in detail in the next graphs (868 MHz, 2.4 GHz and 5 GHz). (b) Insertion losses of thermally sintered microstrip lines (100°C, 160°C and 200°C) and electrically sintered lines (OCP = 0.4 A and 0.6 A) at the three selected frequencies. (c) Insertion losses as a function of final sintering temperature at the three selected frequencies. (d) Insertion losses as a function of waveform slope during electrical sintering averaging to all studied OCP values at the three selected frequencies.

TABLE 3. Insertion losses.

Sintering method	868 MHz	2.4 GHz	5 GHz
Thermal, T_{final}=100 ºC	0.34 ± 0.009	0.568 ± 0.006	0.78 ± 0.07
Thermal, T_{final}=160 ºC	0.19 ± 0.03	0.33 ± 0.03	0.55 ± 0.05
Thermal, T_{final}=200 ºC	0.138 ± 0.005	0.2557 ± 0.0013	0.45 ± 0.03
Electrical, OCP=0.4 A	0.131 ± 0.014	0.27 ± 0.04	0.48 ± 0.04
Electrical, OCP=0.6 A	0.128 ± 0.006	0.267 ± 0.021	0.47 ± 0.03

Insertion losses (dB/mm) of thermally sintered microstrip lines (100 °C, 160 °C and 200 °C) and electrically sintered lines (OCP=0.4 A and 0.6 A) at the three selected frequencies (868 MHz, 2.4 GHz and 5 GHz).

sintering temperature. The reason for this outcome is that the printed structures were not fully sintered using such a low temperature, resulting in a poor conductivity in both DC and RF frequencies (enhancing the ohmic losses) as compared to the rest of sintered lines. Insertion losses are significantly reduced in the case of higher sintering temperature such as 160 °C, but still higher than measured losses for electrical sintered lines. It is only at the highest sintering temperature of 200 °C when insertion losses are similar or even lower than some electrically sintered microstrips (see Fig. 7c). Although electrically sintered lines present lower resistivity, given their high surface roughness, their insertion losses are similar to the 200 °C thermally sintered lines.

FIGURE 8. Numerical simulations and experimental measurements of transmission coefficient S_{21} per unit length for different microstrip lines and sintering processes.

There are opposite effects between both features (resistivity and surface roughness) that provide the similar RF performance shown in Fig. 7a. Fig. 7d depicts the insertion losses trends as a function of the applied voltage slope in the electrical sintering averaging to all analyzed OCP. We can observe lower losses for lower voltage slopes, in agreement

with lower resistivities (see Fig. 6b) and, therefore, lower ohmic losses.

Nevertheless, the differences in losses between thermal sintering at 200 °C and electrical sintering are minor. The abrupt change in resistance during electrical curing process does not degrade the RF behavior of the lines in the analyzed frequency range as it would be expected due to mechanical stress of the line caused by an accelerated heating and showed as lines with higher surface roughness. Therefore, we can take advantage of the benefits that electrical sintering offers over thermal sintering maintaining suitable RF performance.

IV. CONCLUSION

The electrical DC, surface and RF characteristics of inkjet-printed microstrip lines containing silver nanoparticles were studied after thermal and electrical sintering processes under different conditions. Regarding thermally sintered printed patterns, we have demonstrated that lower resistivity values are achieved if the heating treatment is done with temperature step rather than temperature ramp. In both cases, resistivity decreases with heating temperature. For the same sintering time, resistivity shows about 67% decrease when final temperature is 200 °C compared to the final temperature of 100 °C. The best resistivity value of 9.4 $\mu\Omega \cdot$ cm, which is approximately six times the value of bulk silver resistivity, was achieved with a temperature step of 200 °C. Electrical sintering was tested to overcome the limitations of thermal sintering, particularly the long sintering times. With this sintering method, we succeeded in improving the resistivity values down to an average of 3.6 $\mu\Omega \cdot$ cm, which is only 2.3 times higher than that of bulk silver. Surface characterization was carried out to assess the effect of the sintering conditions on the printed structures. While a relatively flat surface was derived from the thermal curing process, higher surface roughness was obtained as a result of current flows during electrical sintering. In average, roughness increased by 63% from thermal sintering to electrical sintering with an OCP of 0.4 A, and by 249 % in the case of 0.6 A. Finally, RF performance of printed microstrip lines was also tested to study the potential impact of the sintering method at RF and microwave frequencies. Our investigations into this area proved that curing by thermal treatment derived in higher insertion losses for sintering temperatures lower than 200 °C, while the differences between thermal sintering at high temperatures and electrical sintering were minor because the higher surface roughness effect was compensated with a lower resistivity. These results suggest that we could make use of the advantages that offer electrical sintering over thermal curing without relinquishing their applicability at the analyzed frequencies.

REFERENCES

[1] MarketsandMarkets. (2016). *Printed Electronics Market by Material (Ink, Substrate), Technology (Inkjet, Screen, Gravure, Flexographic), Device (Sensors, Displays, Batteries, RFID, Lighting, Photovoltaic) and Geography—Global Forecast to 2022*. [Online]. Available: https://www.marketsandmarkets.com/Market-Reports/printed-electronics-market-197.html

[2] S. Khan, L. Lorenzelli, and R. S. Dahiya, "Technologies for printing sensors and electronics over large flexible substrates: A review," *IEEE Sensors J.*, vol. 15, no. 6, pp. 3164–3185, Jun. 2015.

[3] J. A. Mayer, B. Gallinet, T. Offermans, I. Zhurminsky, and R. Ferrini, "Self-contained optical enhancement film for printed photovoltaics," *Sol. Energy Mater. Sol. Cells*, vol. 163, pp. 51–57, Apr. 2017.

[4] D. Li, W.-Y. Lai, Y.-Z. Zhang, and W. Huang, "Printable transparent conductive films for flexible electronics," *Adv. Mater.*, vol. 30, p. 1704738, Jan. 2018.

[5] J. Chen and C. T. Liu, "Technology advances in flexible displays and substrates," *IEEE Access*, vol. 1, pp. 150–158, 2013.

[6] J. F. Salmerón *et al.*, "Properties and printability of inkjet and screen-printed silver patterns for RFID antennas," *J. Electron. Mater.*, vol. 43, no. 2, pp. 604–617, Feb. 2014.

[7] P. Escobedo *et al.*, "Flexible passive near field communication tag for multigas sensing," *Anal. Chem.*, vol. 89, no. 3, pp. 1697–1703, Feb. 2017.

[8] R. Singh, E. Singh, and H. S. Nalwa, "Inkjet printed nanomaterial based flexible radio frequency identification (RFID) tag sensors for the Internet of nano things," *RSC Adv.*, vol. 7, no. 77, pp. 48597–48630, Oct. 2017.

[9] Q. Liu, H. Li, and Y.-F. Yu, "A versatile flexible UHF RFID tag for glass bottle labelling in self-service stores," *IEEE Access*, vol. 6, pp. 59065–59073, 2018.

[10] G. Mattana and D. Briand, "Recent advances in printed sensors on foil," *Mater. Today*, vol. 19, no. 2, pp. 88–99, Mar. 2016.

[11] Y. S. Rim, S.-H. Bae, H. Chen, N. De Marco, and Y. Yang, "Recent progress in materials and devices toward printable and flexible sensors," *Adv. Mater.*, vol. 28, no. 22, pp. 4415–4440, Jun. 2016.

[12] M. E. Morales-Rodríguez, P. C. Joshi, J. R. Humphries, P. L. Fuhr, and T. J. Mcintyre, "Fabrication of low cost surface acoustic wave sensors using direct printing by aerosol inkjet," *IEEE Access*, vol. 6, pp. 20907–20915, 2018.

[13] K. Myny *et al.*, "A thin-film microprocessor with inkjet print-programmable memory," *Sci. Rep.*, vol. 4, no. 1, May 2015, Art. no. 7398.

[14] X. Guo, Y. Hang, Z. Xie, C. Wu, L. Gao, and C. Liu, "Flexible and wearable 2.45 GHz CPW-fed antenna using inkjet-printing of silver nanoparticles on pet substrate," *Microw. Opt. Technol. Lett.*, vol. 59, no. 1, pp. 204–208, Jan. 2017.

[15] M. A. Andersson, A. Özçelikkale, M. Johansson, U. Engström, A. Vorobiev, and J. Stake, "Feasibility of ambient RF energy harvesting for self-sustainable M2M communications using transparent and flexible graphene antennas," *IEEE Access*, vol. 4, pp. 5850–5857, 2016.

[16] R. Kumar, J. Shin, L. Yin, J.-M. You, Y. S. Meng, and J. Wang, "All-printed, stretchable Zn-Ag_2O rechargeable battery via hyperelastic binder for self-powering wearable electronics," *Adv. Energy Mater.*, vol. 7, no. 8, p. 1602096, Apr. 2017.

[17] A. Kaur and P. Chahal, "RF characterization of NiO and TiO_2 based metal-insulator-metal (MIM) diodes on flexible substrates," *IEEE Access*, vol. 6, pp. 55653–55660, 2018.

[18] G. Mattana, A. Loi, M. Woytasik, M. Barbaro, V. Noël, and B. Piro, "Inkjet-printing: A new fabrication technology for organic transistors," *Adv. Mater. Technol.*, vol. 2, no. 10, p. 1700063, 2017.

[19] S.-P. Chen, H.-L. Chiu, P.-H. Wang, and Y.-C. Liao, "Inkjet printed conductive tracks for printed electronics," *ECS J. Solid State Sci. Technol.*, vol. 4, no. 4, pp. P3026–P3033, Feb. 2015.

[20] K.-H. Choi, J. Yoo, C. K. Lee, and S.-Y. Lee, "All-inkjet-printed, solid-state flexible supercapacitors on paper," *Energy Environ. Sci.*, vol. 9, no. 9, pp. 2812–2821, 2016.

[21] A. E. Ostfeld, I. Deckman, A. M. Gaikwad, C. M. Lochner, and A. C. Arias, "Screen printed passive components for flexible power electronics," *Sci. Rep.*, vol. 5, Oct. 2015, Art. no. 15959.

[22] M. Singh, H. M. Haverinen, P. Dhagat, and G. E. Jabbour, "Inkjet printing-process and its applications," *Adv. Mater.*, vol. 22, no. 6, pp. 673–685, 2010.

[23] N. C. Raut and K. Al-Shamery, "Inkjet printing metals on flexible materials for plastic and paper electronics," *J. Mater. Chem. C*, vol. 6, no. 7, pp. 1618–1641, 2018.

[24] A. J. Kell *et al.*, "Versatile molecular silver ink platform for printed flexible electronics," *ACS Appl. Mater. Interfaces*, vol. 9, no. 20, pp. 17226–17237, 2017.

[25] A. Chiolerio, K. Rajan, I. Roppolo, A. Chiappone, S. Bocchini, and D. Perrone, "Silver nanoparticle ink technology: State of the art," *Nanotechnol. Sci. Appl.*, vol. 9, pp. 1–13, Jan. 2016.

[26] S. Mypati, S. R. Dhanushkodi, M. McLaren, A. Docoslis, B. A. Peppley, and D. P. J. Barz, "Optimized inkjet-printed silver nanoparticle films: Theoretical and experimental investigations," *RSC Adv.*, vol. 8, no. 35, pp. 19679–19689, 2018.

[27] S. Wünscher *et al.*, "Simulation and prediction of the thermal sintering behavior for a silver nanoparticle ink based on experimental input," *J. Mater. Chem. C*, vol. 2, no. 31, pp. 6342–6352, 2014.

[28] M. L. Allen *et al.*, "Electrical sintering of nanoparticle structures," *Nanotechnology*, vol. 19, no. 17, p. 175201, 2008.

[29] S. Wünscher, R. Abbel, J. Perelaer, and U. S. Schubert, "Progress of alternative sintering approaches of inkjet-printed metal inks and their application for manufacturing of flexible electronic devices," *J. Mater. Chem. C*, vol. 2, no. 48, pp. 10232–10261, Sep. 2014.

[30] K. Black, J. Singh, D. Mehta, S. Sung, C. J. Sutcliffe, and P. R. Chalker, "Silver ink formulations for sinter-free printing of conductive films," *Sci. Rep.*, vol. 6, no. 1, Aug. 2016, Art. no. 20814.

[31] J. Niittynen, E. Sowade, H. Kang, R. R. Baumann, and M. Mäntysalo, "Comparison of laser and intense pulsed light sintering (IPL) for inkjet-printed copper nanoparticle layers," *Sci. Rep.*, vol. 5, no. 1, Aug. 2015, Art. no. 8832.

[32] J. Perelaer, M. Klokkenburg, C. E. Hendriks, and U. S. Schubert, "Microwave flash sintering of inkjet-printed silver tracks on polymer substrates," *Adv. Mater.*, vol. 21, no. 47, pp. 4830–4834, 2009.

[33] M. Grouchko, A. Kamyshny, C. F. Mihailescu, D. F. Anghel, and S. Magdassi, "Conductive inks with a 'built-in' mechanism that enables sintering at room temperature," *ACS Nano*, vol. 5, no. 4, pp. 3354–3359, Apr. 2011.

[34] D. A. Roberson, R. B. Wicker, and E. MacDonald, "Ohmic curing of printed silver conductive traces," *J. Electron. Mater.*, vol. 41, no. 9, pp. 2553–2566, Sep. 2012.

[35] M. Hummelgård, R. Zhang, H.-E. Nilsson, and H. Olin, "Electrical sintering of silver nanoparticle ink studied by *in-situ* TEM probing," *PLoS ONE*, vol. 6, no. 2, p. e17209, Feb. 2011.

[36] T. Falat, B. Platek, and J. Felba, "Sintering process of silver nanoparticles in ink-jet printed conductive microstructures—Molecular dynamics approach," in *Proc. 13th Int. Conf. Thermal, Mech. Multi-Phys. Simulation Exp. Microelectron. Microsyst. (EuroSimE)*, 2012, pp. 1–5.

[37] H. Lee *et al.*, "Stepwise current electrical sintering method for inkjet-printed conductive ink," *Jpn. J. Appl. Phys.*, vol. 53, p. 05HC07, Apr. 2014.

[38] M. Allen, A. Alastalo, M. Suhonen, T. Mattila, J. Leppaniemi, and H. Seppa, "Contactless electrical sintering of silver nanoparticles on flexible substrates," *IEEE Trans. Microw. Theory Techn.*, vol. 59, no. 5, pp. 1419–1429, May 2011.

[39] I. E. Stewart, M. J. Kim, and B. J. Wiley, "Effect of morphology on the electrical resistivity of silver nanostructure films," *ACS Appl. Mater. Interfaces*, vol. 9, no. 2, pp. 1870–1876, Jan. 2017.

[40] K. Ryu, Y.-J. Moon, K. Park, J.-Y. Hwang, and S.-J. Moon, "Electrical property and surface morphology of silver nanoparticles after thermal sintering," *J. Electron. Mater.*, vol. 45, no. 1, pp. 312–321, Jan. 2016.

[41] M. T. Rahman, J. McCloy, C. V. Ramana, and R. Panat, "Structure, electrical characteristics, and high-temperature stability of aerosol jet printed silver nanoparticle films," *J. Appl. Phys.*, vol. 120, no. 7, p. 075305, Aug. 2016.

[42] T. Bjorninen, S. Merilampi, L. Ukkonen, P. Ruuskanen, and L. Sydanheimo, "Performance comparison of silver ink and copper conductors for microwave applications," *IET Microw., Antennas Propag.*, vol. 4, no. 9, pp. 1224–1231, 2010.

[43] A. Chiolerio *et al.*, "Ag nanoparticle-based inkjet printed planar transmission lines for RF and microwave applications: Considerations on ink composition, nanoparticle size distribution and sintering time," *Microelectron. Eng.*, vol. 97, pp. 8–15, Sep. 2012.

[44] O. Azucena, J. Kubby, D. Scarbrough, and C. Goldsmith, "Inkjet printing of passive microwave circuitry," in *IEEE MTT-S Int. Microw. Symp. Dig.*, Jun. 2008, pp. 1075–1078.

[45] V. Camarchia *et al.*, "Demonstration of inkjet-printed silver nanoparticle microstrip lines on alumina for RF power modules," *Organic Electron.*, vol. 15, no. 1, pp. 91–98, Jan. 2014.

[46] B. Shao, R. Weerasekera, L.-R. Zheng, R. Liu, W. Zapka, and P. Lindberg, "High frequency characterization of inkjet printed coplanar waveguides," in *Proc. 12th IEEE Workshop Signal Propag. Interconnects*, May 2008, pp. 1–4.

[47] M. M. Belhaj, W. Wei, E. Pallecchi, C. Mismer, I. Roch-Jeune, and H. Happy, "Inkjet printed flexible transmission lines for high frequency applications up to 67 GHz," in *Proc. 44th Eur. Microw. Conf.*, 2014, pp. 1528–1531.

[48] K.-H. Jung, S.-W. Kim, M.-K. Maeng, D. G. Kam, and S.-B. Jung, "RF characteristics of flexible circuits patterned with hybrid Ag paste," *J. Mater. Sci. Mater. Electron.*, vol. 29, no. 6, pp. 5074–5081, Mar. 2018.

[49] M. Walther, A. Ortner, H. Meier, U. Löffelmann, P. J. Smith, and J. G. Korvink, "Terahertz metamaterials fabricated by inkjet printing," *Appl. Phys. Lett.*, vol. 95, no. 25, p. 251107, Dec. 2009.

[50] R. Moro, M. Bozzi, S. Kim, and M. Tentzeris, "Novel inkjet-printed substrate integrated waveguide (SIW) structures on low-cost materials for wearable applications," in *Proc. 42nd Eur. Microw. Conf.*, 2012, pp. 72–75.

[51] A. Rida, L. Yang, R. Vyas, and M. M. Tentzeris, "Conductive inkjet-printed antennas on flexible low-cost paper-based substrates for RFID and WSN applications," *IEEE Antennas Propag. Mag.*, vol. 51, no. 3, pp. 13–23, Jun. 2009.

[52] V. Lakafosis, A. Rida, R. Vyas, L. Yang, S. Nikolaou, and M. M. Tentzeris, "Progress towards the first wireless sensor networks consisting of inkjet-printed, paper-based RFID-enabled sensor tags," *Proc. IEEE*, vol. 98, no. 9, pp. 1601–1609, Sep. 2010.

[53] V. Sanchez-Romaguera *et al.*, "Towards inkjet-printed low cost passive UHF RFID skin mounted tattoo paper tags based on silver nanoparticle inks," *J. Mater. Chem. C*, vol. 1, no. 39, pp. 6395–6402, 2013.

[54] P. Escobedo, M. A. Carvajal, L. F. Fernández-Salmerón, J. Fernández-Salmerón, A. Martínez-Olmos, and A. J. Palma, "Passive UHF RFID tag for multispectral assessment," *Sensors*, vol. 16, no. 7, p. 1085, Jul. 2016.

[55] H. Saghlatoon, T. Björninen, L. Sydänheimo, M. M. Tentzeris, and L. Ukkonen, "Inkjet-printed wideband planar monopole antenna on cardboard for RF energy-harvesting applications," *IEEE Antennas Wireless Propag. Lett.*, vol. 14, pp. 325–328, 2015.

[56] V. Sanchez-Romaguera *et al.*, "Inkjet printed paper based frequency selective surfaces and skin mounted RFID tags: The interrelation between silver nanoparticle ink, paper substrate and low temperature sintering technique," *J. Mater. Chem. C*, vol. 3, no. 9, pp. 2132–2140, 2015.

[57] D. M. Pozar, *Microwave Engineering*, 4th ed. Hoboken, NJ, USA: Wiley, 2012.

[58] D. A. Roberson, R. B. Wicker, L. E. Murr, K. Church, and E. MacDonald, "Microstructural and process characterization of conductive traces printed from Ag particulate inks," *Materials*, vol. 4, no. 12, pp. 963–979, May 2011.

[59] S. Jang, D. J. Lee, D. Lee, and J. H. Oh, "Electrical sintering characteristics of inkjet-printed conductive Ag lines on a paper substrate," *Thin Solid Films*, vol. 546, pp. 157–161, Nov. 2013.

[60] D. R. Lide, "Electrical resistivity of pure metals," in *CRC Handbook of Chemistry and Physics*, 87th ed. Boca Raton, FL, USA: Taylor & Francis, 2007.

[61] J. R. Greer and R. A. Street, "Thermal cure effects on electrical performance of nanoparticle silver inks," *Acta Mater.*, vol. 55, no. 18, pp. 6345–6349, Oct. 2007.

[62] G. Vandevenne *et al.*, "A study on the thermal sintering process of silver nanoparticle inkjet inks to achieve smooth and highly conducting silver layers," *Phys. Status Solidi*, vol. 213, no. 6, pp. 1403–1409, Jun. 2016.

[63] S. Merilampi, T. Laine-Ma, and P. Ruuskanen, "The characterization of electrically conductive silver ink patterns on flexible substrates," *Microelectron. Rel.*, vol. 49, no. 7, pp. 782–790, 2009.

[64] O. Kravchuk, Y. Bobitski, and M. Reichenberger, "Electrical sintering of inkjet printed sensor structures on plyimide substrate," in *Proc. IEEE 36th Int. Conf. Electron. Nanotechnol. (ELNANO)*, Apr. 2016, pp. 104–106.

[65] C. Werner, D. Godlinski, V. Zöllmer, and M. Busse, "Morphological influences on the electrical sintering process of Aerosol Jet and Ink Jet printed silver microstructures," *J. Mater. Sci. Mater. Electron.*, vol. 24, no. 11, pp. 4367–4377, Nov. 2013.

[66] R. A. Pucel, D. J. Massé, and C. P. Hartwig, "Losses in microstrip," *IEEE Trans. Microw. Theory Techn.*, vol. MTT-16, no. 6, pp. 342–350, Jun. 1968.

PABLO ESCOBEDO was born in Jaén, Spain, in 1989. He received degrees in telecommunication engineering and electronics engineering from the University of Granada, Granada, Spain, in 2012 and 2013, respectively, the master's degree in computer and network engineering in 2014, and the Ph.D. degree in design and development of printed sensor systems on flexible substrates from the University of Granada. He is currently a Post-Doctoral Researcher with the ECsens Group, Department of Electronics and Computer Technology, University of Granada, where his work is focused on printed and flexible electronics with special interest in sensors and RFID technology.

MIGUEL A. CARVAJAL was born in Granada, Spain, in 1977. He received the M.Sc. degree in physics and the M.Sc. degree in electronic engineering from the University of Granada, in 2000 and 2002, respectively, and the Ph.D. degree in electronic engineering from the University of Granada, in 2007, about the development of a dosimeter system based on commercial MOSFETs. He currently works as a tenured Professor with the University of Granada. His research interests include the effects of irradiation and post-irradiation in MOSFET transistors, RFID tags with sensor capabilities, gas sensor and electrochemiluminescent sensors, and their applications to handheld instrumentation.

JESÚS BANQUERI was born in Jaen, Spain, in 1965. He received the B.S. and M.Sc. degrees in physics from the University of Granada, Spain, in 1988, and the Ph.D. degree from the University of Granada. He is currently a Full Professor with the University of Granada. Since 1989, he has been working in modeling and characterization of MOS transistors in the whole range of temperature with emphasis in the study of the degradation of electron mobility and other parameters as a consequence of high electric field. From 2000, in the interdisciplinary group ECsens, his current research interests are devoted to design, development, and fabrication of sensors and portable electronic instrumentation for environmental, biomedical, and food analysis and monitoring.

ANTONIO MARTÍNEZ-OLMOS was born in Granada, Spain, in 1980. He received the M.Sc. and Ph.D. degrees in electronic engineering from the University of Granada, Granada, in 2003 and 2009, respectively. He is currently an Associate Professor with the University of Granada. His current research interests include the design of tomography sensors and the study of optical sensors for different biological measurements.

LUIS FERMÍN CAPITÁN-VALLVEY received the B.Sc. and Ph.D. degrees in chemistry from the Faculty of Sciences, University of Granada, Spain, in 1973 and 1986, respectively. In 1983, he founded the Solid Phase Spectrometry Group (GSB) and, in 2000, together with Prof. P. López, the interdisciplinary group ECsens, which includes chemists, physicists, and electrical and computer engineers, at the University of Granada. He is currently a Full Professor of analytical chemistry with the University of Granada. His work has produced nearly 350 peer-reviewed scientific papers, 6 books, 25 book chapters, and 6 patents. His current research interests include design, development, and fabrication of sensors and portable instrumentation for environmental, health, and food analysis and monitoring. Recently, he is interested in printing chemical sensor and capillary-based microfluidic devices.

ALBERTO J. PALMA received the B.S. and M.Sc. degrees in physics, in 1991, and the Ph.D. degree, in 1995, from the University of Granada, Granada, Spain. He is currently a Full Professor with the Department of Electronics and Computer Technology, University of Granada. Since 1992, he has been working on trapping of carriers in different electronic devices (diodes and MOS transistors), including characterization and simulation of capture cross sections, random telegraph noise, and generation–recombination noise in devices. From 2000, in the interdisciplinary group ECsens, his current research interests are devoted to design, development, and fabrication of sensors and portable electronic instrumentation for environmental, biomedical, and food analysis and monitoring. Recently, he is working on printing sensors on flexible substrates with processing electronics using inkjet and screen-printing technologies.